A 64×64-Pixels Digital Silicon Photomultiplier Direct TOF Sensor With 100-MPhotons/s/pixel Background Rejection and Imaging/Altimeter Mode With 0.14% Precision Up To 6 km for Spacecraft Navigation and Landing

Matteo Perenzoni, *Member, IEEE*, Daniele Perenzoni, *Member, IEEE*, and David Stoppa, *Senior Member, IEEE*

Abstract—This paper describes a 64×64-pixel 3-D imager based on single-photon avalanche diodes (SPADs) for long-range applications, such as spacecraft navigation and landing. Each 60-μm pixel includes eight SPADs combined as a digital silicon photomultiplier, a triggering logic for photons temporal correlation, a 250-ps 16-b time-to-digital converter, and an intensity counter, with an overall 26.5% fill factor. The sensor provides time-of-flight and intensity information even with a background intensity up to 100 MPhotons/s/pixel. The sensor can work in imaging (short range, 3-D image) and altimeter (long range, single point) modes, achieving up to 300-m and 6-km maximum distance with <0.2-m and <0.5-m precision, respectively, consuming less than 100 mW.

Index Terms—3-D camera, CMOS, digital silicon photomultiplier (d-SiPM), image sensor, LIDAR, silicon photomultiplier, single-photon avalanche diodes (SPADs), time-of-flight (TOF), time-to-digital converter (TDC).

I. INTRODUCTION

THREE-DIMENSIONAL (3-D) imaging is a key enabling technology needed in order to bring environment awareness to devices, appliances, robots, transportation means, and last but not least, spacecrafts, all of which aim at becoming more and more autonomous during their operation. Several ranging techniques are available, but optical ranging demonstrated in the recent years to be superior in terms of depth and lateral resolution with respect to other nonoptical methods, such as ultrasonic and radar, taking advantage of the tremendous development and growing of the image sensor market.

The potential applications, however, differ largely on the requirements they set for the 3-D imaging system, in terms of speed, resolution (lateral and depth), cost, illumination system and probing wavelength, adopted optical ranging technique, power budget, and system size. In particular, operations of spacecraft navigation and landing require typically long range

operation, robustness against background light, and reliable high-speed acquisition without motion artifacts. Among the existing active optical methods, the interferometry technique exploits coherent light and the interference pattern it produces in order to achieve extremely high ranging precision. At the same time, its main limitation is set by the wavelength, giving rise to a very limited depth range [1]. Triangulation-based technique uses the geometrical relationship between the light source and the camera (active triangulation) or between multiple cameras (stereo vision). Again, there is a limitation in the maximum achievable range, which is set by the baseline parameter, i.e., the lateral distance between the optical elements of the system [2], [3]. A mixed approach between triangulation and time-of-flight (TOF) can overcome this limit but geometrically prevents the implementation of imaging arrays [4].

On the other hand, TOF techniques can adapt to a broad variety of scenarios by measuring directly [direct TOF (DTOF)] or indirectly [indirect TOF (ITOF)] the delay between the light pulses emitted by a suitable illuminator and the received backscattered light detected by the sensor. The ITOF is based on in-pixel photodemodulators, and it is an advantageous choice for high-resolution short-range 3-D imaging [5]–[7]. Taking into account the challenges of long range, rejection to background light, and negligible motion artifacts of our target application, it becomes clear that the DTOF technique presents several advantages against the ITOF. In fact, as far as the long range is of concern, the ITOF distance nonambiguity is related to the illuminator modulation frequency, which inevitably sets also the precision [8]. The use of multiple modulation frequencies partly solves this tight tradeoff but with a considerable increase of system complexity [9]. On the other hand, the DTOF requires properly setting the range and resolution of the time measurement and the maximum distance is only limited by the optical power budget. Rejection of background light in conditions of long distance range represents a major performance limitation: indeed, the longer the echo takes to return to the sensor, the higher is the quantity of undesired light that can be captured by the sensor, increasing the noise floor. The DTOF can be advantageous, whenever it is possible to perform smart thresholding on the received pulse, in combination with

time-gating if the approximate range is known [10]. The ITOF, on the contrary, needs to continuously integrate the demodulated signal for the whole integration time. Finally, motion artifacts have to be avoided when the spacecraft is moving: the ITOF requires the acquisition of two, or preferably four frames (one for each 90° phase shift). Therefore, it is unavoidable that moving objects cause artifacts when recombining single phases together in order to reconstruct the 3-D image, since they can be acquired at different target distances. The DTOF, while still requiring several acquisitions in order to produce a relevant statistics, keeps constant the operating conditions (i.e., pulse relative delay), reducing artifacts. The potentially faster acquisition time and a proper pixel histogram processing, for example recognizing multiple peaks due to motion, can enable reduction of distance motion blur.

The implementation of the DTOF for the flash LIDAR system involves the capability of resolving the arrival time of the light echo on a per-pixel basis. Although avalanche photodiodes could potentially be employed, the high-sensitivity readout chain required for fast charge integration and thresholding makes the approach nonpractical for pixel arrays. Single-photon avalanche diodes (SPADs), thanks to the intrinsic early conversion to the digital domain, allow for fast and efficient thresholding and excellent timing performance [11], [12]. In the last few years, several SPAD-based sensors have been proposed for different applications, including TOF [13]–[16]. However, the dark-count rate (DCR) of CMOS SPADs is such that, for long-range applications, it cannot be neglected. Moreover, in the presence of high background levels, pixels implemented with a single SPAD have a high probability of receiving the echo during the SPAD dead time caused by unwanted photons, thus creating pileup effect distortion. The use of multiple SPADs [17] with a correlation logic considerably improved the rejection to undesired counts [18]; the required circuitry area, however, limits the implementation to few pixels making image scanning necessary.

In this paper, an image sensor featuring a compact pixel architecture able to realize photon correlation in time is described. Each pixel implements a digital silicon-photomultiplier (d-SiPM): in the specific case, eight SPADs provide a stream of pulses on a single output, each one corresponding to an avalanche event. The d-SiPM is coupled to a smart triggering logic for concurrent events detection, enabling timestamping, and counting of correlated photons only for improved reliability of distance measurement even in the presence of strong background. This paper extends the work of [19], providing additional circuitry details and measurements.

This paper is organized as follows. In Section II, the system level challenges are addressed in order to explain the requirements, while the chosen architecture is explained in detail in Section III. Section IV shows the complete experimental characterization, and finally, conclusions are drawn.

II. System Level Requirements

In order to avoid unnecessary multiplication of the hardware, the range imaging system has to be designed in such a way that it can perform the altimetry measurement,
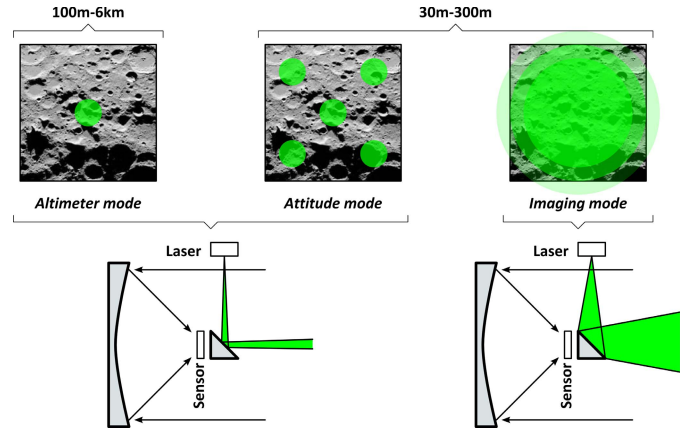

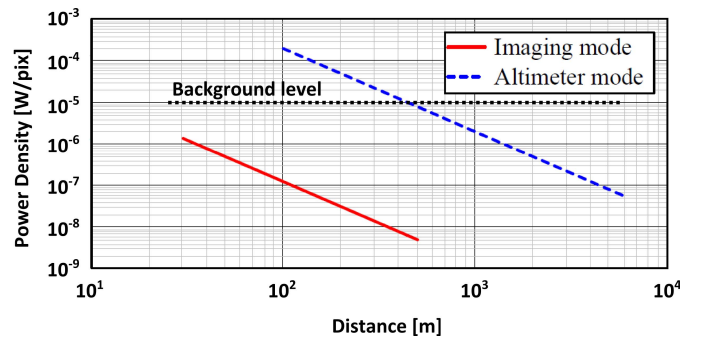Fig. 1. Different system operations to be performed during the navigation and landing.

Fig. 2. Expected optical power impinging on a $60 \times 60 \ \mu m^2$ pixel for the altimeter and imaging mode.

necessary during the navigation toward the target celestial body, but also measuring the attitude (i.e., measurement of the orientation with respect to the target surface) and 3-D imaging operation during the descent and landing phases. As shown in Fig. 1, altimetry and attitude are performed by collimating the laser in a single spot or multiple spots, while 3-D imaging is achieved with diffuse illumination, achievable through a reconfigurable illuminating optics. On the other hand, the sensor has to operate in the range 100 m up to 6 km for the altimetry, while from 30 to 300 m for attitude and 3-D imaging, with a huge variation in the power density of the returned echo.

With the envisaged system specifications, including kilowatt-range high-power laser at 532-nm wavelength and low F-number telescope optics, the expected echo power density can be extracted with the hypothesis of a 0.5 albedo (i.e., diffuse reflectivity) of the target surface. Fig. 2 shows the calculated values, clearly showing the wide range of intensities that spans in excess of four decades (more than 80 dB): this means that the sensor will be working from a situation of strong photon pileup, down to a photon-starved power budget. Reconfigurable operation and programmability are, therefore, a mandatory sensor's feature.

Background light requirements are determined by the use of a narrow-band filter with 532-nm center wavelength, considering 0.5 albedo and 30° of sun elevation angle, and result in a maximum impinging flux of 100 MPhotons/s/pixel.
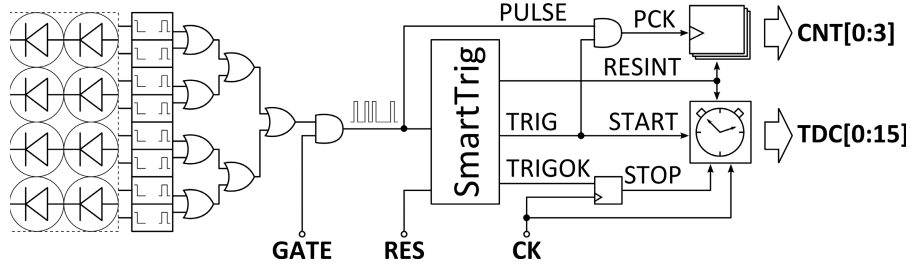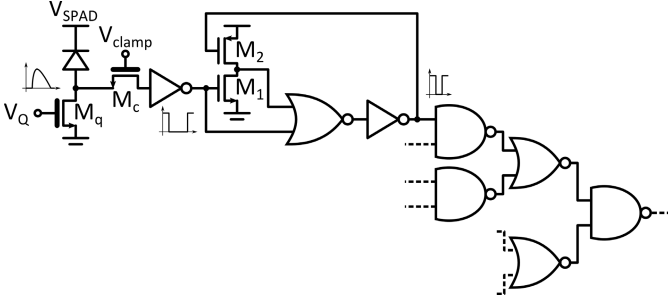
Fig. 3. Pixel block diagram.

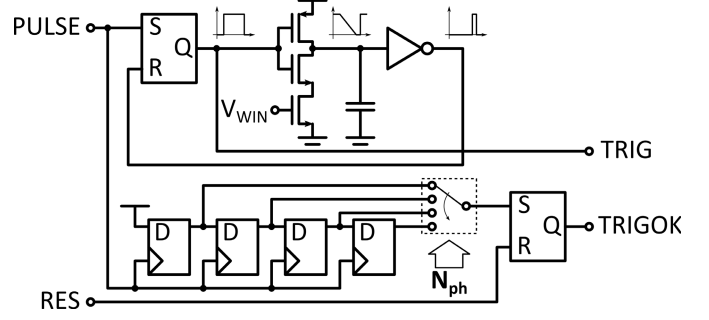Fig. 4. Detailed schematic of the d-SiPM with front-end, pulse-compression monostable, and OR-tree.

Fig. 5. Schematic of the smart triggering logic with rolling window generation.

III. 3-D IMAGER ARCHITECTURE AND OPERATION

The main building block of the sensor is the pixel, which acts autonomously during the observation time by identifying the laser echo and producing timestamps and photons counts when the events are recognized. In the following, the pixel is explained in detail, and then the whole chip architecture is described.

A. Pixel Schematic

Fig. 3 shows the pixel high-level schematic, highlighting the digital control signals GATE, CK, and RES, and the outputs CNT [0:3] and time-to-digital converter (TDC) [0:15]. As shown, the pixel contains eight SPADs (similar SPAD structures have been described and characterized in [20] and [21]) with their respective frontend circuitry, each one fed into a monostable and then into an OR-tree, as shown in detail in Fig. 4. The purpose of this circuitry is to compress the SPAD pulse from the typical 10–100 ns due to recharge (dead time) to much less than 1 ns, and then to combine pulses from different SPADs on a single line [22], [23], obtaining a d-SiPM with a photon detection bandwidth that can be in the order of 10^9 ph/s. This is fundamental for the recognition of photons hitting the pixel closely in time, in order to distinguish the potential echo from dark counts and background. The SPAD frontend is composed by quenching and clamping thick-oxide transistors, in order to properly recharge the SPAD with a maximum 3.3 V excess bias, and clamp safely the pulse to 1.8 V as required by the following circuitry; the clamping transistor has to be biased at a voltage V_{clamp} at least one threshold voltage larger than the inverter threshold, so as to avoid entering the triode region. The feedback-based monostable reliably generates very short pulses, with duration set by the two-gate delays plus a safe margin that can be imposed by design by tuning M_2 aspect ratio: in this

design, it has been set to approximately 260 ps. Monte Carlo simulations predict a standard deviation of 17 ps, which is low enough to guarantee the pulse generation. In order to save area, the OR-tree is realized with a cascade of NOR–NAND gates.

The resulting stream of pulses is then processed by a smart triggering logic, that, depending on the setting of the number of correlated photons N_{ph}, identifies whether $N > N_{ph}$ photons are falling within a rolling time window of duration T_{WIN}. As shown in Fig. 5, this is accomplished with an asynchronous monostable realized with an unbalanced current-starved inverter, producing a pulse having its width inversely proportional to the current controlled by V_{WIN}. Simultaneously, each pulse shifts a logic "1" in the shift register, initialized with zero values, and the programmed selector connects the desired stage to an SR latch. When N_{ph} or more photons are detected, a trigger validation (TRIGOK) is generated; otherwise, the whole pixel is reset and waits for another SPAD pulse.

Eventually, a counter and a TDC process and store, respectively, the number of photons detected within the time window (for the evaluation of the albedo), and the time of arrival of the first photon (for the DTOF measurement). Once the pixel recognizes a relevant event, it completes the acquisition, freezing its state until an external reset is applied. The TDC architecture shown in Fig. 6 has been realized with two operating modes selectable by the CHAIN signal, in order to fulfill the range requirements for the altimetry and imaging cases. With CHAIN = 0, the TDC operates in the "high-speed" mode through the ring oscillator, by counting the periods of a nominal 4-GHz oscillation frequency on a total of 7 b, completing the LSB of the TDC1 byte with the ring oscillator output. At the same time, the TDC2 byte contains the number of clock cycles since the start of the acquisition. Given that TDC1 measures the time from the first detected photon to the first CK rising edge, the time of arrival can be computed as TDC2 × FS1 – TDC1, with FS1 the full-scale value of
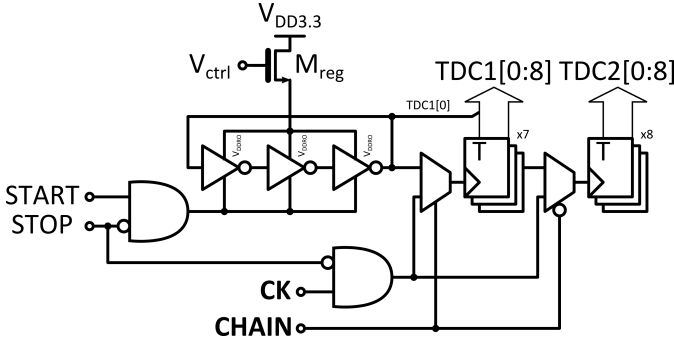
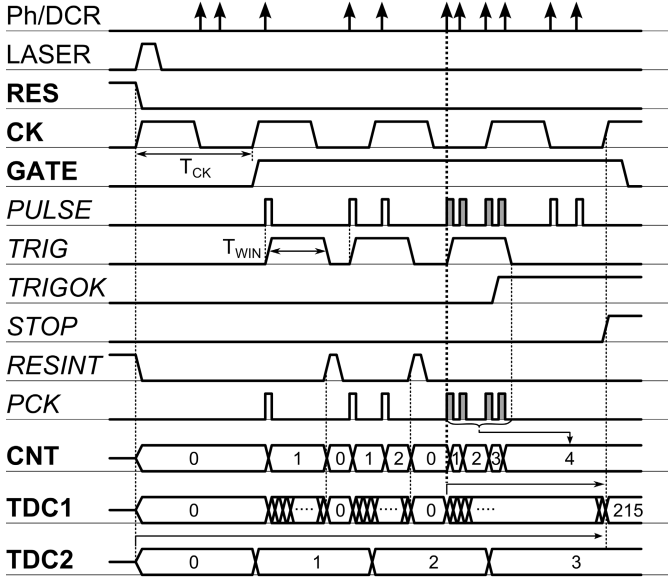Fig. 6. Schematic of the 16-b dual mode TDC (counter- and ring-oscillator-based).

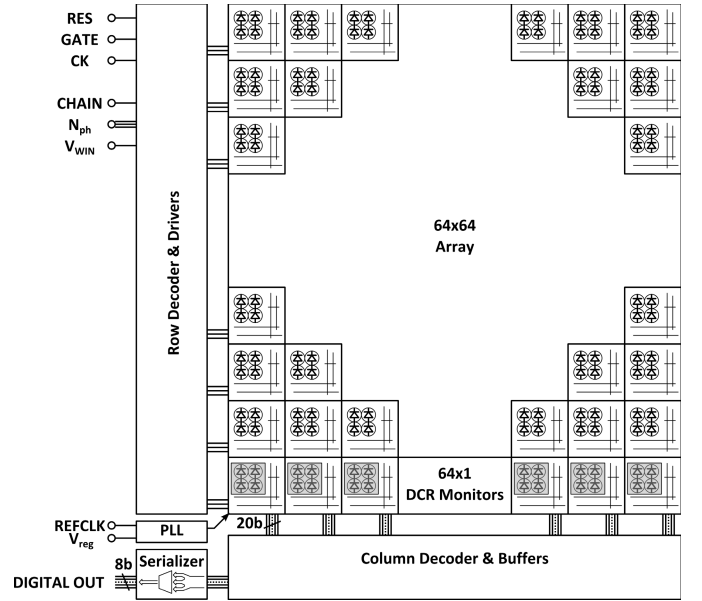Fig. 7. Timing diagram showing the typical pixel operation with $N_{ph} = 3$.

Fig. 8. Chip architecture showing the peripheral circuitry and the additional row for DCR monitoring and testing.

pulses, which are too sparse in time and that do not reach N_{ph} within the time window identified by the self-generated TRIG signal. However, TDC1 is started immediately in order to preserve the time information carried by the leading edge of the returning light pulse, ignoring the result only in the case of nonvalidation. In particular, in the discarded event case, a fast internal reset RESINT restores the pixel for a new detection. In the case of detected event, the signal TRIGOK acts as a validation signal, and so the counter stores the number of photons occurred within T_{WIN} (which can be larger than N_{ph}), and the TDC is stopped on the first available rising edge of CK. As shown in the example of Fig. 7, if the validation occurs in the subsequent clock period, the fine TDC measurement can be longer than T_{CK}, and this has to be taken into account in the definition of the TDC range and the clock period.

B. Chip Periphery and Readout

The overall chip architecture is shown in Fig. 8. The focal plane comprises the 64×64 TOF pixels array, plus an additional row of DCR monitors recording in a local 8-b counter the overall counts of the d-SiPM during the observation time. Half of the pixels in this row are shielded with the top metal layer in order to evaluate the DCR independently from the impinging light and can be used by the controlling system to adjust parameters like the SPAD bias voltage, for example. Moreover, some test points are probed for characterization and debugging purposes.

The row decoder includes, beside addressing circuitry, the digital drivers for the distribution of the CK, GATE, and RES signals to the whole array. During readout, each pixel delivers the TDC (16 b) and counter (4 b) data on a 20-b columnwise vertical bus; the values on the selected column are buffered on a horizontal bus that enters a byte serializer, splitting the 20-b word in three parts on an 8-b bus, with zero padding for the extra bits. Additionally, also the whole 20-b word is connected to output pads for a potential

TDC1 within the clock period. When CHAIN = "1," the two counters are chained together and the TDC simply counts the number of clock cycles, allowing for coarser but longer TOF measurement using 15 b (the LSB of TDC1 byte has to be ignored as the ring oscillator is not started). The TDC conversion time lasts few nanoseconds, needed to complete the counter settling, and therefore at the sensor level, it is limited by the readout time. The CK signal frequency can be changed accordingly to the operating mode in order to properly set the desired range. Nominally, the circuit has been designed to operate with a $T_{CK} = 25$ ns and $T_{LSB} = 250$ ps in fast mode, and with a $T_{CK} = 10$ ns for the slow mode. Therefore, the maximum TOF for the fast mode is 6.4 μs (≈ 970 m) and 327.7 μs (≈ 50 km) for the slow mode, largely including the target specifications. The TDC quantization in terms of distance therefore results in 3.8 cm and 1.5 m, respectively. The real distance resolution of the TOF system depends on the collected statistics (histogram) and on the employed algorithm to extract the distance [24], and is generally better than the TDC resolution thanks to interpolation.

The timing diagram of Fig. 7 shows in detail a typical operation cycle of a pixel with $N_{ph} = 3$ and the TDC operating in fast mode. It can be seen that avalanches occurring before the activation of the GATE signal are discarded, as well as
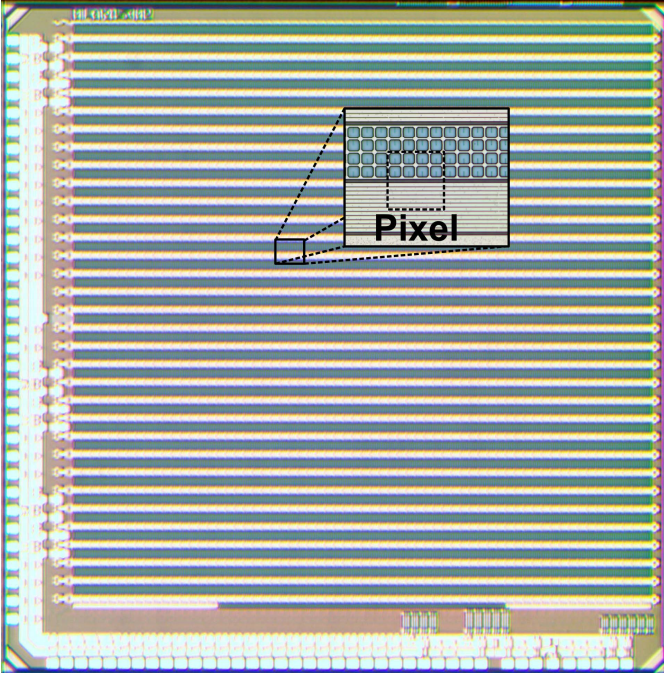
Fig. 9.   Chip micrograph with magnification on the pixel region, showing the eight SPADs and the pixels arranged in alternating vertically flipped pattern.

Fig. 10.   Cumulative DCR map for a typical chip at different excess bias values.

20-b parallel readout. The outputs are designed to work at 100-MHz speed, which, including the settling time from the pixel to the column decoder, gives a 64×64 pixel readout time of 135 μs for the 8-b parallel output and 54 μs for the 20-b parallel output. Considering the maximum TOF for the altimeter mode (40 μs) and for the imaging mode (2 μs), the maximum frame rate results 10.6 and 17.9 kfps, respectively.

The control voltage V_{ctrl} of the TDCs can be either provided externally or connected to the PLL V_{reg}. The PLL contains a replica of the TDC, a 360° phase comparator, and a charge pump feeding V_{reg}, where externally a lead–lag loop filter has to be connected. The TDC replica is continuously running, and only the frequency generated by the most-significant bit is used in the loop. The use of the PLL for V_{ctrl} generation allows canceling process, voltage and temperature variations, locking the TDCs to a known reference [25]: the residual deviations are given by the pixel to pixel nonuniformity between TDCs and can be compensated with one-time calibration of the individual full-scale values.

IV. EXPERIMENTAL RESULTS

The designed chip has been fabricated with a standard 0.15-μm 6M CMOS technology (micrograph of Fig. 9). The pixel, of 60-μm pitch and 26.5% fill-factor, is arranged in an alternating vertically flipped pattern in order to share the SPADs' deep n-well implant, thus minimizing dead areas between rows. In order to limit the crosstalk between SPADs, which may introduce artifacts, a conservative width has been chosen [21]. The chip has been fully characterized from the electrical and optical point of view, using digital acquisition and generation boards controlled through a custom LabVIEW program. Although the 100-MHz readout has been already proved with an FPGA controller, which will be used for the
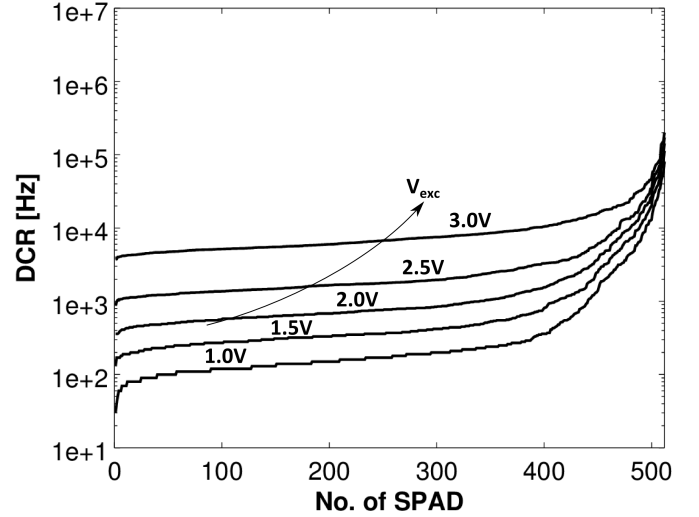
final prototype, for the sake of flexibility, measurements have been taken at the reduced rate of 10 MHz due to the very high loading (several hundreds of picofarads) of the available digital acquisition boards.

A. SPAD Characterization

The DCR monitors row enabled several measurements on the SPAD devices themselves, as the 20-b lines could also be used to extract single SPAD outputs. By measuring the count rate varying the SPAD bias voltage, it was possible to measure a breakdown voltage $V_{BD} = 18.8$ V and, therefore, to extract the DCR maps for the 64×8 pixels of a representative chip. Results are shown in Fig. 10 for various excess bias values, highlighting a sudden increase for $V_{exc} > 3.0$ V, most probably due to the beginning of secondary breakdown effects; at $V_{exc} = 3.0$ V, which is the chosen operating point, the median DCR results 6.8 kHz.

The availability of SPAD pulses also allowed tuning the quench voltage V_Q in order to keep the dead time to about 100 ns, thus minimizing the afterpulsing probability.

B. Triggering and TDC Characterization

The smart triggering logic and the TDCs can be characterized with the use of the d-SiPM DCR as a uniform source of pulses in time, provided that the event rate is low enough so that there is no distortion: indeed, being DCR events driven by Poisson statistics, the time of arrival is described by an exponential function, which can be approximated by a constant when the probability of having an event is very low (i.e., <10%). A code density test on the fine TDC (TDC1) in high-speed mode showed a differential nonlinearity (DNL), oscillating regularly between −0.4 and 0.5 LSB, which translates into a deformation of the time histogram with the time bin of even codes being larger, approximately 2.4 times, than the time bin of odd codes. This systematic error comes from the unbalanced threshold of the latches that are sampling and digitizing the ring oscillator value. The correction factor has been characterized as a single number for the whole chip:
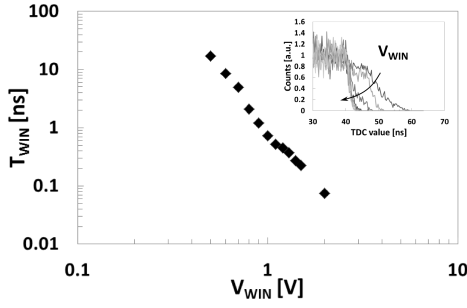
Fig. 11. Indirect measurement of the smart trigger time window versus V_{WIN}. Inset: TDC histograms at different time window durations.

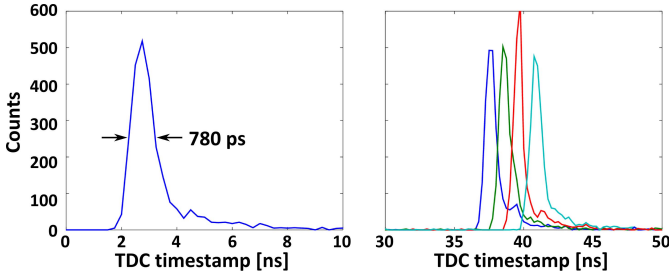
Fig. 12. Characterization of the pixel timing performance, showing a total of 780-ps FWHM of jitter and good linearity across the TDC2 digit change.
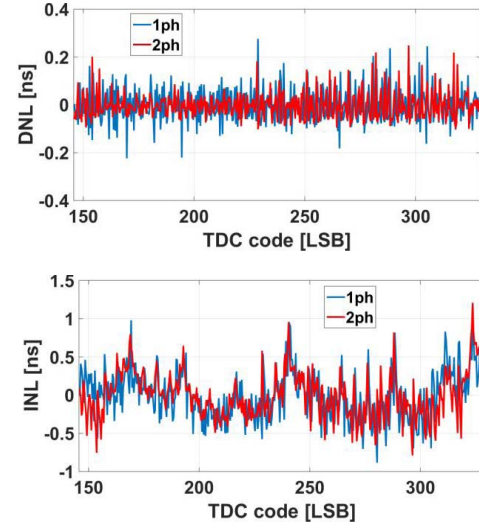

Fig. 13. DNL and INL of the pixel using subcode peak extraction for a representative portion of the measurement range with $N_{ph} = 1, 2$.

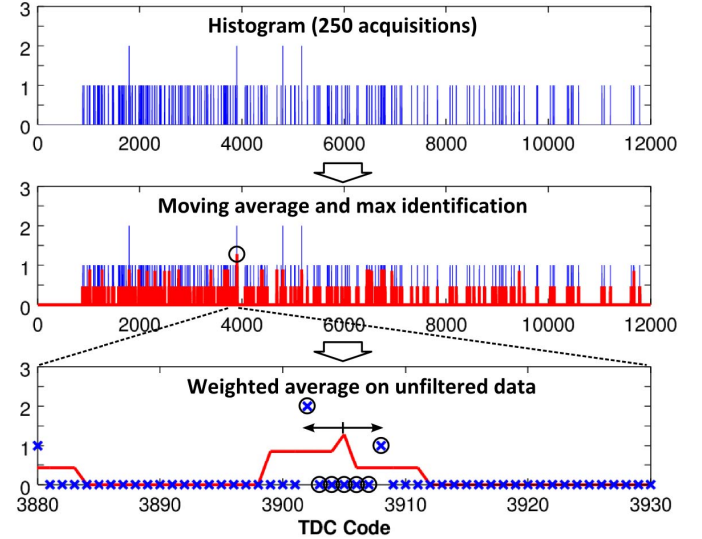Fig. 14. Description of the reference algorithm adopted to extract the distance measurement starting from the 250-points histogram.

while the single timestamp cannot be corrected, a histogram can be instead calibrated, thus avoiding wrong estimation of the TOF. All the measurements presented in this paper include this correction.

The width of the smart trigger window can be tested by considering that, using multiple photons, the timestamps distribution changes from the ideally rectangular shape to a trapezoidal shape with the additional width determined by T_{WIN} itself, due to photons falling across two clock cycles. Capturing the TDC histograms again with the DCR only, with $N_{ph} = 2$ and $T_{CK} = 40$ ns, at various values of V_{WIN} allowed us to obtain the measurement of Fig. 11, useful for setting the desired window duration.

C. Timing Measurements

By shining a 70-ps full-width half-maximum (FWHM) laser at 470-nm wavelength on the sensor, it is possible to evaluate the overall pixel performance in terms of time resolution and linearity. Fig. 12 shows the histograms obtained on a single pixel: on the left side, it is possible to extract the total jitter of 780-ps FWHM. This value comprises the SPAD and the front-end jitter, the TDC jitter, and the OR-tree paths nonuniformity, which are the dominant contribution. On the right side, the laser pulse has been delayed in such a way that it falls across the digit change of TDC2, with $T_{CK} = 40$ ns, and acquired several times with 1-ns spacing in time: it is possible to see how the linearity in time is well preserved (represented by the constant distance of the pulses), and the only macroscopic effect is a slightly unbalanced time-of-arrival attribution to the previous clock cycle. No artifacts, such as double peaks or missing codes, demonstrate the seamless interpolation between the TDC1 and TDC2 values.

By performing more accurately the same measurement and extracting the laser peak position by fitting the values near the maximum of the histogram, it is possible to quantitatively extract the deviation in terms of DNL and integral nonlinearity (INL) of the overall TOF measurement. A 50-ns portion of the whole range, slightly more than one clock cycle, including two TDC2 transitions (at codes 160 and 320), has been scanned in time with 100-ps steps of the laser pulse delay. The measurement has been repeated for both $N_{ph} = 1$ and 2, and the result in terms of INL and DNL is shown in Fig. 13: no relevant discontinuity is visible at the clock cycle transitions, and the linearity performance is preserved at different numbers of photon validation N_{ph}.

D. Time-of-Flight Measurements

In order to emulate in a laboratory environment the distance and laser echo attenuation similar to the real scenario,
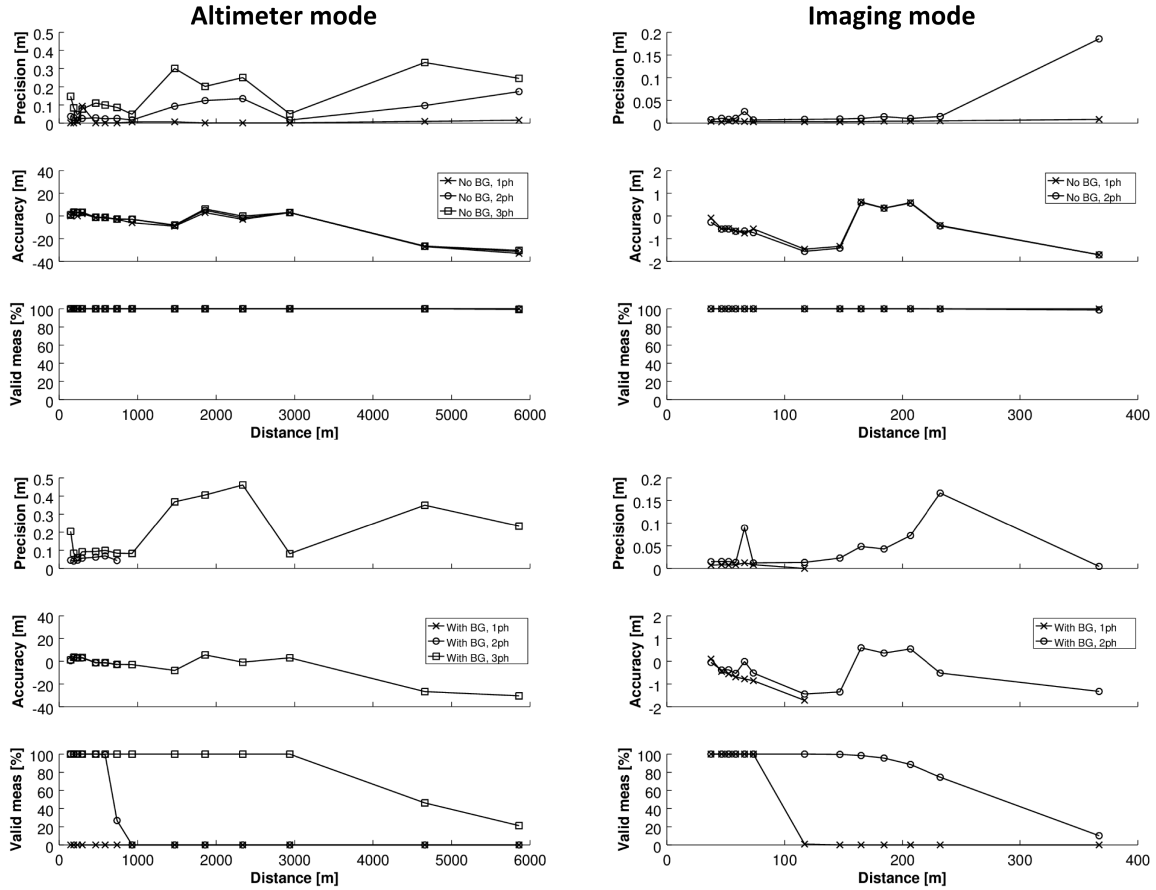
Fig. 15.   Emulated distance measurement, without and with 100 MPhotons/s/pixel background light, for both altimeter and imaging modes.

the power density of Fig. 2 has been reproduced with an optical setup comprising a set of neutral density filters (NDFs) and a programmable delay generator. The envisaged high-power laser parameters have been used in order to correct the different SPAD responsivities at the given wavelengths, pulse width, and peak power, with the hypothesis of 0.5 albedo; then, for each of the NDF and delay combinations, several distance measurements have been performed, using different N_{ph} settings, with and without an emulated background light of 100 MPhotons/s/pixel. The background has been emulated with a tunable light source, calibrated with the use of several unshielded pixels in the DCR monitors line in order to reach the expected count rate obtained from the calculations. A single distance measurement is composed by 250 single-frame acquisitions in order to build per-pixel histograms: Fig. 14 shows the reference algorithm used to extract the distance value, starting from a 250-points histogram. The first operation is the filtering of the histogram data with a moving average followed by a rough estimation of the laser position by finding its maximum. Subsequently, the algorithm computes finely the centroid by using a weighted average on the original histogram by exploiting the estimated maximum position (circles indicate the data selected from the original histogram, used to compute the weighted average). Both the altimetry and imaging modes have been evaluated, using, respectively, the low-speed ("chain" TDC mode) and high-speed timestamping. The altimetry measurements are the result

of a 2×2 pixel binning, as this is the expected spot size of the collimated beam on the focal plane.

All the results are summarized in Fig. 15, showing the precision (repeatability, 1σ), the accuracy with respect to the ideal distance, and the number of valid measurements (the percentage of histograms where it was possible to reliably determine the peak position). Analyzing these results in detail, it appears clear that without background light, the detection of the first event, being it, a photon or DCR ($N_{ph} = 1$), is sufficient to extract the distance, as the histogram is typically free from spurious counts. A relatively small amount of DCR events are present, but do not influence significantly the measurement, because the observation time is in the microseconds order, while the DCR amounts to several kilohertzes. At the same time, enabling multiple photons smart triggering gives the same results in terms of accuracy, while precision results worsened. This is an expected result, because the number of captured events on 250 acquisitions measurements decreases, and therefore the population available for the interpolation is smaller. When the same measurement is performed with the background light, the results show an inversion: the distance obtained with $N_{ph} = 1$ is reliable only for very near targets, while the algorithm fails to recover the pulse position as soon as the light echo decreases, falling below the background noise floor. On the other hand, triggering with two or even three photons allows obtaining valid measurements up to the maximum range, with an acceptable precision
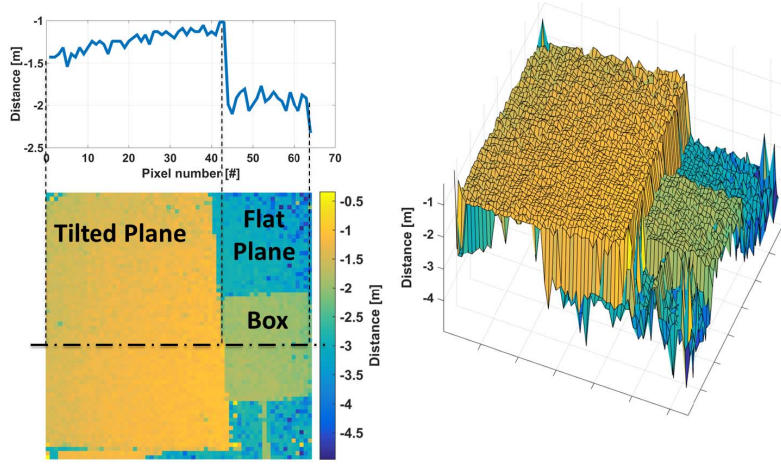
Fig. 16.   Example of a range image obtained with 30k points histograms.

TABLE I
SUMMARY OF THE SENSOR PERFORMANCE

Parameter	Note	Value	Unit
Chip characteristics			
Array resolution		64×64 pixels	
Technology		CMOS 150nm 6M	
Chip size		4.4×4.4	mm^2
Pixel pitch		60	μm
Pixel fill-factor		26.5	%
SPAD bias voltage	V_{exc}=3.0V	21.8	V
SPAD median DCR	V_{exc}=3.0V	6.8	kHz
TDC resolution	Imaging mode	250	ps
	Altimeter mode	20	ns
TDC depth	Imaging mode	16	bit
	Altimeter mode	15	bit
Max frame rate (1pt)	Imaging mode	17.9	kfps
At 100MHz readout	Altimeter mode	10.6	kfps
Power consumption	Digital 1.8V, 3.3V	47.7	mW
	SPAD 21.8V	45.8	mW
Emulated distance measurement performance			
Frame rate (250 pts)	Imaging mode	7.68	fps
At 10MHz readout	Altimeter mode	7.16	fps
Distance range	Imaging mode	367	m
	Altimeter mode	5862	m
Precision (σ)	Imaging mode	<0.2	m
		<0.13	%
	Altimeter mode	<0.5	m
		<0.14	%
Accuracy	Imaging mode	<1.5	m
		<0.37	%
	Altimeter mode	<35	m
		<1.9	%
Background flux		100	Mph/s/pix

and with comparable accuracy. The accuracy in the altimeter mode is limited by the clock period, which is quantizing the TOF measurement: with more measurement points, a periodic pattern would be visible, function of the relative position of the echo with respect to the clock cycle; worsened precision can also occur when the laser echo falls in between two clock cycles.

In order to demonstrate range imaging on a reduced scale, an optical setup with flood scene illumination and standard camera optics on the sensor has been prepared. Due to the limited power of the available laser, the power density on the scene results to be approximately 10^{-2} times the expected value on the larger distance for the imaging

mode. Therefore, the range measurement is the result of the acquisition of 30k points in order to restore an equivalent SNR. The obtained image with setting $N_{ph} = 2$ is shown in Fig. 16, and demonstrates the quality of the image potentially achievable in the final system at 300 m distance, resolving features in the order of fractions of meters.

Table I summarizes the results of the whole characterization, concerning the chip characteristics and the emulated distance measurement test. Power consumption, which is dependent on the operating conditions, has been measured with the chip operating in imaging mode, with the strong background conditions applied.

V. Conclusion

A dual-mode DTOF sensor satisfying the requirements of long range (30–300 m and 100 m–6 km) and rejection of background light up to 100 MPhotons/s/pixel has been developed, exploiting an architecture able to identify on a pixel basis the temporal correlation between multiple photons. Range measurements with precision at the maximum distance better than 50 cm for the altimeter mode and 20 cm for the imaging mode has been demonstrated, even in presence of the maximum admitted background light level. The 64×64-pixels prototype imaging capabilities have also been demonstrated in a scaled setup. Future works include the realization of a scaled system prototype with high power laser and on the long term, space irradiation test and the increase of the imager resolution are foreseen.

Acknowledgments

References

[1] P. Seitz, "Quantum-noise limited distance resolution of optical range imaging techniques," *IEEE Trans. Circuits Syst. I, Reg. Papers*, vol. 55, no. 8, pp. 2368–2377, Sep. 2008.

[2] M.-C. Amann, T. Bosch, M. Lescure, R. Myllyla, and M. Rioux, "Laser ranging: A critical review of usual techniques for distance measurement," *Opt. Eng.*, vol. 40, no. 1, pp. 10–19, Jan. 2001.

[3] Y. Oike, M. Ikeda, and K. Asada, "A 375×365 high-speed 3-D range-finding image sensor using row-parallel search architecture and multisampling technique," *IEEE J. Solid-State Circuits*, vol. 40, no. 2, pp. 444–453, Feb. 2005.

[4] O. Sgrott, D. Mosconi, M. Perenzoni, G. Pedretti, L. Gonzo, and D. Stoppa, "A 134-pixel CMOS sensor for combined time-of-flight and optical triangulation 3-D imaging," *IEEE J. Solid-State Circuits*, vol. 45, no. 7, pp. 1354–1364, Jul. 2010.

[5] S.-M. Han, T. Takasawa, T. Akahori, K. Yasutomi, K. Kagawa, and S. Kawahito, "A 413×240-pixel sub-centimeter resolution time-of-flight CMOS image sensor with in-pixel background canceling using lateral-electric-field charge modulators," in *IEEE ISSCC Dig. Tech. Papers*, Feb. 2014, pp. 130–131.

[6] S.-J. Kim, J. D. K. Kim, S.-W. Han, B. Kang, K. Lee, and C.-Y. Kim, "A 640×480 image sensor with unified pixel architecture for 2D/3D imaging in 0.11 μm CMOS," in *Proc. IEEE Symp. VLSI Circuits*, Jun. 2011, pp. 92–93.

[7] S.-J. Kim, B. Kang, J. D. K. Kim, K. Lee, C.-Y. Kim, and K. Kim, "A 1920×1080 3.65 μm-pixel 2D/3D image sensor with split and binning pixel structure in 0.11 μm standard CMOS," in *IEEE ISSCC Dig. Tech. Papers*, Feb. 2012, pp. 396–398.

[8] F. Remondino and D. Stoppa, Eds., *TOF Range-Imaging Cameras*, Berlin, Germany: Springer-Verlag, 2013.

[9] A. Payne *et al.*, "A 512×424 CMOS 3D time-of-flight image sensor with multi-frequency photo-demodulation up to 130 MHz and 2 GS/s ADC," in *IEEE ISSCC Dig. Tech. Papers*, Feb. 2014, pp. 134–135.

[10] J. Kostamovaara *et al.*, "On laser ranging based on high-speed/energy laser diode pulses and single-photon detection techniques," *IEEE Photon. J.*, vol. 7, no. 2, Apr. 2015, Art. no. 7800215.

[11] C. Veerappan *et al.*, "A 160×128 single-photon image sensor with on-pixel 55ps 10b time-to-digital converter," in *IEEE Int. Solid-State Circuits Conf. (ISSCC) Dig. Tech. Papers*, Feb. 2011, pp. 312–314.

[12] S. Jahromi, J. Jansson, I. Nissinen, J. Nissinen, and J. Kostamovaara, "A single chip laser radar receiver with a 9×9 SPAD detector array and a 10-channel TDC," in *Proc. Eur. Solid-State Circuits Conf. (ESSCIRC)*, Graz, Austria, 2015, pp. 364–367.

[13] R. J. Walker, J. A. Richardson, and R. K. Henderson, "A 128×96 pixel event-driven phase-domain $\Delta\Sigma$-based fully digital 3D camera in 0.13 μm CMOS imaging technology," in *Proc. ISSC*, 2011, pp. 410–412.

[14] F. Villa *et al.*, "CMOS imager with 1024 SPADs and TDCs for single-photon timing and 3-D time-of-flight," *IEEE J. Sel. Topics Quantum Electron.*, vol. 20, no. 6, Nov./Dec. 2014, Art. no. 3804810.

[15] N. A. W. Dutton, L. Parmesan, A. J. Holmes, L. A. Grant, and R. K. Henderson, "320×240 oversampled digital single photon counting image sensor," in *Proc. IEEE Symp. VLSI Circuits*, Jun. 2014, pp. 1–2.

[16] M. Perenzoni, N. Massari, D. Perenzoni, L. Gasparini, and D. Stoppa, "A 160×120 pixel analog-counting single-photon imager with time-gating and self-referenced column-parallel A/D conversion for fluorescence lifetime imaging," *IEEE J. Solid-State Circuits*, vol. 51, no. 1, pp. 155–167, Jan. 2016.

[17] L. H. C. Braga *et al.*, "A fully digital 8×16 SiPM array for PET applications with per-pixel TDCs and real-time energy output," *IEEE J. Solid-State Circuits*, vol. 49, no. 1, pp. 301–314, Jan. 2014.

[18] C. Niclass, M. Soga, H. Matsubara, S. Kato, and M. Kagami, "A 100-m range 10-frame/s 340×96-pixel time-of-flight depth sensor in 0.18-μm CMOS," *IEEE J. Solid-State Circuits*, vol. 48, no. 2, pp. 559–572, Feb. 2013.

[19] M. Perenzoni, D. Perenzoni, and D. Stoppa, "A 64×64-pixel digital silicon photomultiplier direct ToF sensor with 100 Mphotons/s/pixel background rejection and imaging/altimeter mode with 0.14% precision up to 6 km for spacecraft navigation and landing," in *Proc. IEEE Int. Solid-State Circuits Conf. (ISSCC)*, San Francisco, CA, USA, Jan./Feb. 2016, pp. 118–119.

[20] L. Pancheri, G.-F. Dalla Betta, L. H. C. Braga, H. Xu, and D. Stoppa, "A single-photon avalanche diode test chip in 150 nm CMOS technology," in *Proc. Int. Conf. Microelectron. Test Struct. (ICMTS)*, Udine, Italy, 2014, pp. 161–164.

[21] H. Xu, L. Pancheri, L. H. C. Braga, G.-F. D. Betta, and D. Stoppa, "Cross-talk characterization of dense single-photon avalanche diode arrays in CMOS 150-nm technology," *Opt. Eng.*, vol. 55, no. 6, p. 067102, Jun. 2016.

[22] L. H. C. Braga *et al.*, "An 8×16-pixel 92k SPAD time-resolved sensor with on-pixel 64ps 12b TDC and 100 MS/s real-time energy histogramming in 0.13 μm CIS technology for PET/MRI applications," in *IEEE ISSCC Dig. Tech. Papers*, Feb. 2013, pp. 486–487.

[23] N. A. W. Dutton *et al.*, "A time-correlated single-photon-counting sensor with 14 GS/s histogramming time-to-digital converter," in *IEEE ISSCC Dig. Tech. Papers*, Feb. 2015, pp. 204–205.

[24] K. Q. K. Nguyen, E. M. D. Fisher, A. J. Walton, and I. Underwood, "An experimentally verified model for estimating the distance resolution capability of direct time of flight 3D optical imaging systems," *Meas. Sci. Technol.*, vol. 24, no. 12, p. 125001, 2013.

[25] J. Richardson *et al.*, "A 32×32 50ps resolution 10 bit time to digital converter array in 130 nm CMOS for time correlated imaging," in *Proc. IEEE Custom Integr. Circuits Conf.*, Sep. 2009, pp. 77–80.

Matteo Perenzoni (M'09) received the Laurea degree in electronics engineering from the University of Padova, Padova, Italy, in 2002.

In 2002, he was with the University of Padova, where he joined the mixed-signal integrated circuit design for channel decoding. Since 2004, he has been with the Integrated Radiation and Image Sensors Research Unit, Center for Materials and Microsystems, Fondazione Bruno Kessler, Trento, Italy, as a Researcher. From 2006 to 2010, he was collaborating on teaching courses of electronics and sensors with NanoMicro Master, Trento, Italy. In 2011, he was a Director of the biannual optoelectronics and photonics Winter School co-organized with the University of Trento, Trento. During 2014, he was a Visiting Research Scientist in the terahertz Sensing Group with the Technical University of Delft, Delft, Netherlands. His current research interests include the design of advanced vision sensors for visible, X-ray, infrared, and terahertz, and modeling and optimization of analog integrated circuits.

Mr. Perenzoni has been a member of the Technical Program Committee of the European Solid-State Circuit Conference since 2015.

Daniele Perenzoni (M'16) received the master's degree in electronic engineering from the University of Padova, Padova, Italy, in 2012.

In 2009, he joined the Integrated Radiation and Imaging Sensors (IRIS) Research Unit, Fondazione Bruno Kessler for his master's thesis work concerning terahertz chip design. From 2010, he was with the Quadra s.r.l., Trento, Italy, as an Electronic Technician and a Programmer Expert. In 2011, he rejoined IRIS Unit as a Technician. His current research interests include PCB design, measurement tasks, and research support.

David Stoppa (M'97–SM'12) received the Laurea degree in electronics engineering from the Politecnico of Milan, Milan, Italy, in 1998, and the Ph.D. degree in microelectronics from the University of Trento, Trento, Italy, in 2002.

Since 2000, he has been a Faculty Member with the Telecommunications Engineering Faculty, University of Trento, Trento, where has been involved in teaching the courses of analog electronics and microelectronics. He was a Group Leader of the Smart Optical Sensors and Interfaces Group, Fondazione Bruno Kessler, from 2010 to 2013. He has been a Research Scientist with Fondazione Bruno Kessler, since 2002, where he is currently the Head of the Integrated Radiation and Image Sensors Research Unit. He has authored or co-authored over 100 papers in international journals and presentations at international conferences. He holds several patents in the field of image sensors. His current research interests include the field of CMOS integrated circuits design, image sensors, and biosensors.

Dr. Stoppa received the 2006 European Solid-State Circuits Conference Best Paper Award. Since 2011, he has served as a Program Committee Member of the International Solid-State Circuits Conference and the SPIE Videometrics, Range Imaging, and Application Conference, and he has served as the Technical Committee Member of the International Image Sensors Workshop in 2009, 2013, and 2015.